A SCALABLE SPHERE-CONSTRAINED MAGNITUDE-SPARSE SAR IMAGING

MING JIANG[1,*], JIAXUAN QU[1], JINSHAN DING[1], JINGWEI LIANG[2]

[1]*National Key Laboratory of Radar Signal Processing, Xidian University, Xi'an, China*
[2]*School of Mathematical Sciences and Institute of Natural Sciences, Shanghai Jiao Tong University, Shanghai, China*

Abstract. The classical synthetic aperture radar (SAR) imaging techniques based on matched filters are limited by data bandwidth, resulting in limited imaging performance with side lobes and speckles present. To address the high-resolution SAR imaging problem, sparse reconstruction has been extensively investigated. However, the state-of-the-art sparse recovery methods seldom consider the complex-valued reflectivity of the scene and only recover an approximated real-valued scene instead. Furthermore, iterative schemes associated with the sparse recovery methods demand a high computational cost, which limits the practical applications of these methods. In this paper, we establish a sphere-constrained magnitude-sparsity SAR imaging model, aiming at enhancing the SAR imaging quality with high efficiency. We propose a non-convex non-smooth optimization method, which can be accelerated by stochastic average gradient acceleration to be scalable with large-scale problems. Numerical experiments are conducted with point-target and extended-target simulations. On the one hand, the point-target simulation showcases the superiority of our proposed method over the classical methods in terms of resolution. On the other hand, the extended-target simulation with random phases is considered to be in line with the practical scenario, and the results demonstrate that our method outperforms the classical SAR imaging methods and sparse recovery without phase prior in terms of PSNR. Meanwhile, owing to the stochastic acceleration, our method is faster than the existing sparse recovery methods by orders of magnitude.

Keywords. Non-convex optimization, Sparse recovery; Synthetic aperture radar; Stochastic proximal algorithm.

1. INTRODUCTION

Synthetic aperture radar (SAR) imaging is an advanced imaging technique, and it can be taken by radar mounted to a moving platform, and can provide higher spatial resolution images compared to conventional stationary beam scanning radars [1]. The traditional imaging techniques based on matched filters are simple to use and stable in performance. However, they are limited by the data bandwidth resulting in limited imaging performance with side lobes and speckles present. Since the SAR imaging problem can be formulated as an ill-posed inverse problem, the advent of the compressed sensing (CS) theory [2, 3] has brought a new regime in image recovery. The core of the CS-based methods is to design reconstruction algorithms to recover the underlying image which can be sparsely represented under a certain transformation. In SAR or inverse SAR (ISAR) imaging (ISAR can be regarded as a specific mode of SAR), sparse image reconstruction has been extensively investigated in the last decade [4, 5, 6, 7, 8, 9, 10, 11, 12]. However, these methods are computationally demanding due to the iterative scheme, and high memory burden, which limit its practical application. To tackle this problem, though some efforts have been devoted to a fast approximation of SAR observation [13] and proximal splitting algorithms [14], to name a few, fast scalable sparse imaging methods require further study to

---

meet the practical applications. In addition, the scattering response of a target scene is complex-valued with random phase due to the back-scattering of electromagnetic waves on the heterogeneous materials of the scene. However, the complex-valued scattering is barely considered in sparse SAR imaging. Instead, most sparse SAR recovery methods only recover the real-valued magnitude for simplicity. This is in general an approximation of the scattering but lacks modeling accuracy. To our knowledge, the sparse SAR recovery methods accounting for the phase were only addressed in [10, 11], but the proposed methods were not scalable to large-scale problems.

To properly address the sparse SAR imaging problem, we take the phase information, which is interpreted as the sphere constraint, into account in this article. To this intent, we design a novel sphere-constrained magnitude-sparsity non-convex optimization model and propose a stochastic sPhere-constrained Sparse Imaging (sPSI) method, aiming at enhancing the SAR imaging quality with high efficiency. On the one hand, our proposed non-convex model improves the sparse SAR imaging model with higher accuracy. On the other hand, the stochastic acceleration inspired by stochastic average gradient acceleration (SAGA) [15] and stochastic proximal alternating linearized minimization (sPALM) [16] is able to tackle large-scale problems in practice with orders of magnitude of the improvement in terms of computational cost.

Notation. Before moving to the problem setup, we introduce the notation which will be used hereafter. Matrices and vectors are denoted in boldface uppercase letters and lowercase letters such as $\mathbf{X}$ and $\mathbf{x}$, respectively. The individual entry of a matrix and a vector is denoted in the normal font such as $X_{i,j}$ and x_i, respectively. The notation diag($\cdot$) has different definitions according to the type of the argument. Precisely, diag($\mathbf{x}$) creates a diagonal matrix with the vector $\mathbf{x}$ on the main diagonal, while diag($\mathbf{X}$) gets the main diagonal of the matrix $\mathbf{X}$. For any matrix $\mathbf{X}$, $||\mathbf{X}||_p$ denotes the p-norm of the matrix. Specifically, $||\mathbf{X}||_F$ is called the Frobenius norm of the matrix. In addition, $\odot$ denotes the Hadamard piecewise product and $*$ denotes convolution.

2. SAR imaging problem

In this section, we start with the general SAR imaging model, then present our novel sparse SAR imaging problem with the sphere constraint.
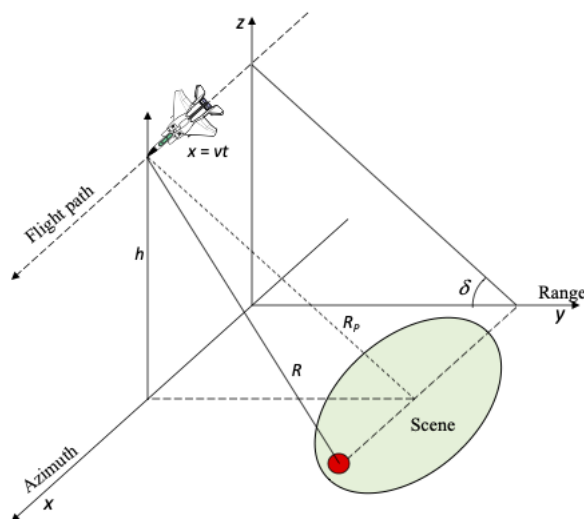

FIGURE 1. Illustration of SAR geometry

2.1. SAR observation model. The illustration for a typical stripmap-mode SAR is shown in Figure 1. The radar platform travels at velocity v in the azimuth direction and transmits pulses during the observation time. Given a scene of interest, a baseband pulse $u(\tau)$ modulated by a carrier frequency f_c yields the transmitted signal

$$s(\tau) = u(\tau) \exp \{j2\pi f_c \tau\}, \tag{2.1}$$

where τ is defined as fast range time, $u(\tau)$ is the envelope of the linear frequency modulation (LFM), which is the most popular choice in SAR, denoted by

$$u(\tau) = \text{rect}(\tau/T_p) \exp \{j\pi\gamma\tau^2\}, \tag{2.2}$$

where $\text{rect}(\cdot)$ is a rectangular function parameterized by pulse duration T_p and chirp rate γ. In the regime of SAR imaging, a sequence of pulses illuminates the object and the back-scattered signals are delayed with respect to the range of the target. Due to the motion of the radar platform, the range of the target varies in terms of slow azimuth time. Thus, given the slow time t and the fast time τ, the demodulated received signal is the superposition of all the back-scattered signals from the whole illuminated scene scaled by the reflectivity function, which can be written as

$$y(\tau, t) = \int \int \sigma(x, y) u \left(\tau - \frac{2R_{x,y}(t)}{c} \right) \exp \left\{ -\frac{j4\pi f_c R_{x,y}(t)}{c} \right\} dxdy, \tag{2.3}$$

where $\sigma(x, y)$ represents the reflectivity coefficient of the target located at (x, y), c is the velocity of the electromagnetic wave, $R_{x,y}(t)$ denotes the range of the target located at (x, y) at slow time t.

2.2. Sphere-constrained sparse SAR imaging. Since the reflectivity is complex-valued, we utilize the exponential form where the amplitude and the phase are decoupled such that

$$\sigma(x, y) = A(x, y) \exp \{j\phi(x, y)\} = A(x, y)P(x, y).$$

If we discretize the fast time and slow time, we can rewrite SAR observation model (2.3) in a linear forward model such that

$$\mathbf{y} = \mathbf{H}(\mathbf{a} \odot \mathbf{p}) + \mathbf{n}, \tag{2.4}$$

where $\mathbf{y} \in \mathbb{C}^{M\times1}$, $\mathbf{a} \in \mathbb{R}^{N\times1}$, $\mathbf{p} \in \mathbb{C}^{N\times1}$, and $\mathbf{n} \in \mathbb{C}^{M\times1}$ stacked in a vector form denote the complex-valued echo data, amplitude and phase of reflectivity of the target scene to be recovered and contaminated Gaussian additive noise, respectively. In addition, $\mathbf{H} \in \mathbb{C}^{M\times N}$ is the sensing matrix of SAR observation incorporated with the down-sampling effect with $M < N$ if in the CS regime. As an example, the $\mathbf{H}$ matrix is generated such that

$$\mathbf{H} = \begin{bmatrix} h(\tau_1, t_1, 1) & h(\tau_1, t_1, 2) & \cdots & h(\tau_1, t_1, N) \\ h(\tau_1, t_2, 1) & h(\tau_1, t_2, 2) & \cdots & h(\tau_1, t_2, N) \\ \vdots & \vdots & \ddots & \vdots \\ h(\tau_1, t_{N_t}, 1) & h(\tau_1, t_{N_t}, 2) & \cdots & h(\tau_1, t_{N_t}, N) \\ h(\tau_2, t_1, 1) & h(\tau_2, t_1, 2) & \cdots & h(\tau_2, t_1, N) \\ \vdots & \vdots & \ddots & \vdots \\ h(\tau_{m_\tau}, t_{n_t}, 1) & h(\tau_{m_\tau}, t_{n_t}, 2) & \cdots & h(\tau_{m_\tau}, t_{n_t}, N) \\ \vdots & \vdots & \ddots & \vdots \\ h(\tau_{M_\tau}, t_{N_t}, 1) & h(\tau_{M_\tau}, t_{N_t}, 2) & \cdots & h(\tau_{M_\tau}, t_{N_t}, N) \end{bmatrix} \tag{2.5}$$

where the entry of $\mathbf{H}$ is expressed by

$$h(\tau_{m_\tau}, t_{n_t}, i) = u\left(\tau_{m_\tau} - \frac{2R_i(t_{n_t})}{c}\right) \exp\left\{-\frac{j4\pi f_c R_i(t_{n_t})}{c}\right\},$$
$$\forall \tau_{m_\tau} = \tau_1, \tau_2, \cdots, \tau_{M_\tau} \tag{2.6}$$
$$\forall t_{n_t} = t_1, t_2, \cdots, t_{N_t}$$

with M_τ and N_t being the number of samplings in fast time and slow time, respectively, yielding the total number of rows $M = M_\tau N_t$. The number of columns N denotes the total number of pixels of the target scene after discretization.

If we consider the CS case, namely $M < N$, then inverse problem (2.4) is ill-posed, and a direct inversion is impossible. In general SAR imaging, due to the limitations of signal bandwidth and synthetic aperture, the imaging performance is limited with side lobes and speckles present. Since we consider complex-valued reflectivity in this paper and the phase exhibits randomness, we leverage the sparse reconstruction technique where the magnitude of the reflectivity is supposed to be sparse to achieve a super-resolved solution. In the case that the scene is not sparse in the direct space, the scene can be sparse in a transformed space such that

$$\mathbf{a} = \mathbf{\Psi}\alpha, \tag{2.7}$$

where α is the sparse representation associated with the dictionary $\mathbf{\Psi}$. Moreover, the synthesis operator $\mathbf{\Psi}$ and the corresponding analysis operator $\mathbf{\Psi}^T$ (or $\mathbf{\Psi}^*$ in complex-valued case) satisfy $\mathbf{\Psi}\mathbf{\Psi}^T = \mathbf{Id}$(or $\mathbf{\Psi}\mathbf{\Psi}^* = \mathbf{Id}$). For instance, the (bi-)orthogonal wavelet space is a good sparse representation for most natural scenes; the analysis operator and the synthesis operator are wavelet transform and inverse wavelet transform, respectively. Furthermore, the exponential form $\mathbf{p}$, which contains the phase information is interpreted as a unit sphere centered at the origin in the complex plane, yielding the unit-norm constraint

$$|\mathbf{p}| = 1. \tag{2.8}$$

Equipped with these magnitude and sphere constraints, problem (2.4) can be transformed to solve an optimization in the synthesis sparsity formulation such that

$$\min_{\alpha, \mathbf{p}} \frac{1}{2}||\mathbf{y} - \mathbf{H}(\mathbf{\Psi}\alpha \odot \mathbf{p})||^2 + \lambda||\alpha||_1 + \iota_{\mathbb{R}_+^N}(\mathbf{\Psi}\alpha) + \iota_{\mathcal{B}^N}(\mathbf{p}), \tag{2.9}$$

where the first term denotes the data fidelity, the ℓ_1-norm represents the sparsity promoting regularization adjusted by the parameter λ, $\iota(\cdot)$ represents the indicator function, defined as

$$\iota_S(x) = \begin{cases} 0, & \text{if } x \in S, \\ +\infty, & \text{otherwise}, \end{cases} \tag{2.10}$$

and specifically, $\iota_{\mathbb{R}_+^N}(\mathbf{\Psi}\alpha)$ expresses the non-negativity constraint imposed on the amplitude of the reflectivity, where $\mathbb{R}_+^N$ denotes the non-negativity subset of N-dimensional real numbers. while $\iota_{\mathcal{B}^N}(\mathbf{p})$ denotes the sphere constraint, where the set $\mathcal{B}^N$ is a complex Stiefel manifold such that $\mathcal{B}^N = \{\mathbf{X} \in \mathbb{C}^N | \mathbf{X}^*\mathbf{X} = \mathbf{I}_N\}$.

3. Stochastic Proximal Alternating Linear Minimization Recovery

In this section, we focus on the solution of the proposed sphere-constrained sparse SAR imaging problem, which is based on the alternating minimization scheme to achieve a high-resolution result with reduced side lobes. Then, to alleviate the high computational cost of the iterative method, a stochastic acceleration technique is incorporated with the proposed imaging method to be scalable with large-scale problems in practice.

3.1. **Sphere-constrained sparse imaging method.** The minimization problem (2.9) is difficult to solve due to its non-convexity and non-smoothness. The general idea is to alternatingly estimate α and $\mathbf{p}$. Then, due to the non-smoothness of the regularizers, we employ a proximal alternating linear minimization (PALM) framework [17], which involves solving two subproblems via the iteration scheme

$$\alpha^{k+1} = \arg\min_{\alpha}\{\frac{1}{2}\|\mathbf{y} - \mathbf{H}(\boldsymbol{\Psi}\alpha \odot \mathbf{p}^k)\|^2 + \lambda\|\mathbf{a}\|_1 + \iota_{\mathbb{R}_+^N}(\boldsymbol{\Psi}\alpha)\}, \tag{3.1}$$

$$\mathbf{p}^{k+1} = \arg\min_{\mathbf{p}}\{\frac{1}{2}\|\mathbf{y} - \mathbf{H}(\boldsymbol{\Psi}\alpha^{k+1} \odot \mathbf{p})\|^2 + \iota_{\mathcal{B}^N}(\mathbf{p})\}, \tag{3.2}$$

where each subproblem is convex but non-smooth. With the help of proximal operators, analytic solutions can be easily found for both subproblems. Thus, the solution of subproblem (3.1) can be achieved by a forward gradient step followed by a backward proximal operation step such that

$$\alpha^{k+1/2} = \alpha^k - \mu_k \nabla_{\alpha} f(\alpha^k, \mathbf{p}^k), \tag{3.3}$$

$$\alpha^{k+1} = \mathcal{S}_{\mu\lambda}\left(\boldsymbol{\Psi}^T \max(\boldsymbol{\Psi}\alpha^{k+1/2}, 0)\right) \tag{3.4}$$

where $f(\alpha, \mathbf{p}) = \frac{1}{2}\|\mathbf{y} - \mathbf{H}(\boldsymbol{\Psi}\alpha \odot \mathbf{p})\|^2$ for the sake of simplicity of writing, $\nabla_{\alpha} f(\alpha, \mathbf{p})$ being the partial derivative of $f(\alpha, \mathbf{p})$ respective to α and $\mu_k = 1/\|\mathbf{H}\operatorname{diag}(\mathbf{p}^k)\|_2$ being the gradient step size estimated on-the-fly. The non-negativity constraint is realized by a projection on the non-negativity orthant and the magnitude-sparsity constraint is realized by a proximal operator $\mathcal{S}$ which denotes the well-known soft-thresholding in case of ℓ_1-norm. Similarly, subproblem (3.2) can also be solved via a forward-backward scheme such that

$$\mathbf{p}^{k+1} = \mathcal{P}_{\mathcal{B}^N}(\mathbf{p}^k - \eta_k \nabla_{\mathbf{p}} f(\alpha^{k+1}, \mathbf{p}^k)), \tag{3.5}$$

where $\nabla_{\mathbf{p}} f(\alpha, \mathbf{p})$ denotes the partial derivative of $f(\alpha, \mathbf{p})$ respective to $\mathbf{p}$ and the gradient step size $\eta_k = 1/\|\mathbf{H}\operatorname{diag}(\alpha^k)\|_2$. As explained in the previous section, the sphere constraint is interpreted as a unit norm condition, which is evaluated by a projection onto a complex Stiefel manifold [18] such that

$$\mathcal{P}_{\mathbf{B}^N}(\operatorname{diag}(\mathbf{p})) = \sum_{i=1}^{N} \mathbf{u}_i \mathbf{v}_i^T, \tag{3.6}$$

where $\mathbf{u}$ and $\mathbf{v}$ are complex unitary vectors from the singular value decomposition of $\operatorname{diag}(\mathbf{p})$, namely $\operatorname{diag}(\mathbf{p}) = \mathbf{U}\boldsymbol{\Sigma}\mathbf{V}^*$. In summary, our sPhere-constrained Sparse Imaging (PSI) method is presented in Algorithm 1.

Algorithm 1: sPhere-constrained Sparse Imaging (PSI)

Input: Sensing matrix $\mathbf{H}$, Observation $\mathbf{y}$;
Output: Reconstructed RCS $(\mathbf{a}, \mathbf{p})$;
Initialize $\alpha^0 \in \mathbb{R}^{N \times 1}$, $\mathbf{p}^0 \in \mathbb{C}^{N \times 1}$;
for $0 \leq k \leq K - 1$ **do**
    $\alpha^{k+1/2} = \alpha^k - \mu_k \nabla_{\alpha} f(\alpha^k, \mathbf{p}^k)$
    $\alpha^{k+1} = \mathcal{S}_{\mu\lambda}\left(\boldsymbol{\Psi}^T \max(\boldsymbol{\Psi}\alpha^{k+1/2}, 0)\right)$
    $\mathbf{p}^{k+1} = \mathcal{P}_{\mathcal{B}^N}(\mathbf{p}^k - \eta_k \nabla_{\mathbf{p}} f(\alpha^{k+1}, \mathbf{p}^k))$
end
$\mathbf{a} = \boldsymbol{\Psi}\alpha^K$, $\mathbf{p} = \mathbf{p}^K$

3.2. **Acceleration by stochastic average gradient.** Due to the large number of samplings in both fast time and slow time and the large number of pixels to recover, it is computationally demanding to calculate the gradient of the loss function, rendering the proposed deterministic optimization algorithm PSI ineffective, which limits the application of iterative-based methods in practical SAR imaging.

To tackle this issue, a randomized version of PSI is proposed. Given a mini-batch $B_k \subset \{1, 2, \cdots, M\}$ with cardinality b, the full estimated gradients $\nabla_{\alpha} f(\alpha^k, \mathbf{p}^k)$ and $\nabla_{\mathbf{p}} f(\alpha^{k+1}, \mathbf{p}^k)$, respectively, are replaced by random estimates $\tilde{\nabla}_{\alpha}(\alpha^k, \mathbf{p}^k)$ and $\tilde{\nabla}_{\alpha}(\alpha^{k+1}, \mathbf{p}^k)$ by selecting only a few gradient samples $\nabla_{\alpha} f_j(\alpha^k, \mathbf{p}^k)$ and $\nabla_{\mathbf{p}} f_j(\alpha^{k+1}, \mathbf{p}^k)$ for $j \in B_k$. Many forms of random estimators can be found in the literature, such as stochastic gradient descent (SGD). However, the standard SGD requires decreasing steps, which is intractable in practice, to ensure the variance of the update direction trending to zero. Thus, to be able to use constant step sizes, we leverage the concept of stochastic gradient descent with variance reduction and employ the stochastic average gradient acceleration (SAGA) [15] for the gradient estimator $\tilde{\nabla}_{\alpha}(\alpha^k, \mathbf{p}^k)$ such that

$$\tilde{\nabla}_{\alpha}(\alpha^k, \mathbf{p}^k) = \frac{1}{b}\Sigma_{j \in B_k}(\nabla_{\alpha} f_i(\alpha^k, \mathbf{p}^k) - g_{k,j}) + \frac{1}{M}\Sigma_{i=1}^{M} g_{k,i}, \qquad (3.7)$$

where

$$g_{k+1,i} = \begin{cases} \nabla_{\alpha} f_i(\alpha^k, \mathbf{p}^k) & \text{if } i \in B_k, \\ g_{k,i} & \text{otherwise.} \end{cases} \qquad (3.8)$$

A similar expression can also be derived for the gradient estimator $\tilde{\nabla}_{\mathbf{p}}(\alpha^{k+1}, \mathbf{p}^k)$. When M is large and $b \ll M$ ($b = 1$ in the extreme case), the computation of SAGA gradient estimator is of orders of magnitude less expensive than computing the full gradient. Built upon the SAGA estimator, our stochastic average gradient acceleration PSI (sPSI) algorithm is presented in Algorithm 2.

In practice, the global Lipschitz constants of the partial gradients of f are usually difficult to estimate. Thus, adaptive step size choice based on estimating local Lipschitz constants is leveraged for sPSI. In general, we find that it is sufficient to estimate on-the-fly in every iteration the Lipschitz constants of the stochastic gradients for the randomly sub-sampled mini-batch. Let estimated Lipschitz constants of the stochastic estimates be $L_{\alpha}(\mathbf{p}^k)$ and $L_{\mathbf{p}}(\alpha^k)$ for the k-th iteration such that

$$L_{\alpha}(\mathbf{p}^k) = ||\mathbf{H}_{B_k} \text{diag}(\mathbf{p}^k)||_2^2, \qquad (3.9)$$

$$L_{\mathbf{p}}(\alpha^k) = ||\mathbf{H}_{B_k} \text{diag}(\alpha^k)||_2^2, \qquad (3.10)$$

where $\mathbf{H}_{B_k}$ denotes the sub-matrix with the random selection of B_k rows of $\mathbf{H}$, then the adaptive step sizes can be set as $\gamma_{1,k} = 1/3L_{\alpha}(\mathbf{p}^k)$ and $\gamma_{2,k} = 1/3L_{\mathbf{p}}(\alpha^k)$ to guarantee the convergence, where more detailed proof can be found in [16]. We also remark that since the non-convex problem is sensitive to the initialization, we can initialize $(\alpha, \mathbf{p})$ with the result of any classical SAR imaging methods to avoid trapping into local minima.

Algorithm 2: Stochastic Average Gradient Accelerated PSI (sPSI)

Input: Sensing matrix $\mathbf{H}$, Observation $\mathbf{y}$;
Output: Reconstructed RCS $(\mathbf{a}, \mathbf{p})$;
Initialize $\alpha^0 \in \mathbb{R}^{N \times 1}$, $\mathbf{p}^0 \in \mathbb{C}^{N \times 1}$;
for $0 \le k \le K - 1$ **do**
    $\alpha^{k+1/2} = \alpha^k - \gamma_{1,k} \tilde{\nabla}_{\alpha}(\alpha^k, \mathbf{p}^k)$
    $\alpha^{k+1} = \mathcal{S}_{\mu\lambda}\left(\mathbf{\Psi}^T \max(\mathbf{\Psi}\alpha^{k+1/2}, 0)\right)$
    $\mathbf{p}^{k+1} = \mathcal{P}_{\mathcal{B}^N}(\mathbf{p}^k - \gamma_{2,k} \tilde{\nabla}_{\mathbf{p}}(\alpha^{k+1}, \mathbf{p}^k))$
end
$\mathbf{a} = \mathbf{\Psi}\alpha^K, \mathbf{p} = \mathbf{p}^K$

---

4. Experiments

In this section, we consider two numerical simulations: 1) point targets simulation to analyze the super-resolution performance of sPSI compared with classical methods and 2) extended targets simulation to show the efficiency of sPSI in terms of imaging quality and computational cost.

4.1. **Point targets experiment.** In this experiment, we showcase the super-resolution ability of sPSI by conducting a point-targets simulation. The simulated scene composed of four point targets is of size 100×100, which represents a physical field of view 464m× 562m. The main parameters of the simulation are reported in Table 1.

We compare sPSI with the classical back projection (BP) method, where the sampling rate satisfies the Nyquist sampling theorem. Both sPSI and BP use the whole data and the imaging results are shown in Figure 2. Note that the point targets are placed adjacently in range and azimuth directions such that the BP method can only separate them by limit. Therefore, in Figure 2(a1), the four points targets are overlapped due to the side lobes so that they are not easy to visually recognize. We can clearly see the main lobes of the targets placed in range and azimuth directions approach significantly causing the ambiguity in Figure 2(b1) and (c1), respectively. Constrained by the Nyquist-sampling theorem, this is the resolution limit of conventional imaging methods subject to the given radar parameters. On the contrary, our proposed sPSI can obtain higher resolution beyond Nyquist theorem shown in Figure 2(a2). This is owing to the fact that sPSI tries to search for the sparsest solution that fits the observation, yielding the side lobes are greatly suppressed and the main lobe is largely sharpened. More precisely, in this simulation, sPSI shows the side lobes below 60 dB in both range and azimuth directions shown in Figure 2(b2) and (c2), respectively, while between 10 dB and 20 dB for the BP method. In addition, by using the sPSI method, the width of the main lobes is only across a few pixels so the width of the main lobe can almost be ignored, while the width of the main lobe at 3 dB for BP is important. Thus, this simulation demonstrates the super-resolution capability and side lobes suppression of our proposed sPSI, compared to the conventional SAR imaging method.

Range	988648 m
Squint angle	0°
Center frequency	5.3 GHz
Bandwidth	3.0111 MHz
Pulse width	41.75 μs
The pulse-repetition frequency	1257 Hz
Sampling frequency in range	3.2317 MHz
Field of view of the scene	(464 m, 562 m)
Number of (Range, Azimuth) samples	(100, 100)

TABLE 1. The parameter settings for point targets simulation.

4.2. **Extended targets experiment.** In this section, we conducted a numerical experiment on a general extended target case. The simulated target scene composed of two ellipses represents a field of view 100 m× 100 m. To simulate the real SAR imaging scenario, we add random phases to the targets, yielding the ground-truth amplitude and the phase shown in Figure 3(g1) and (g2), respectively. The airborne radar was working under stripmap SAR mode and the detailed parameters for the simulation are shown in Table 2. We compare sPSI with 1) the classical BP method, 2) the conventional sparse method (Lasso) without consideration of phase constraint and 3) non-accelerated PSI. Under the given sampling frequency, the target scene was discretized to a (64, 64) grid and the full data is of size 300×300, corresponding to 300 samples for both azimuth and range directions.
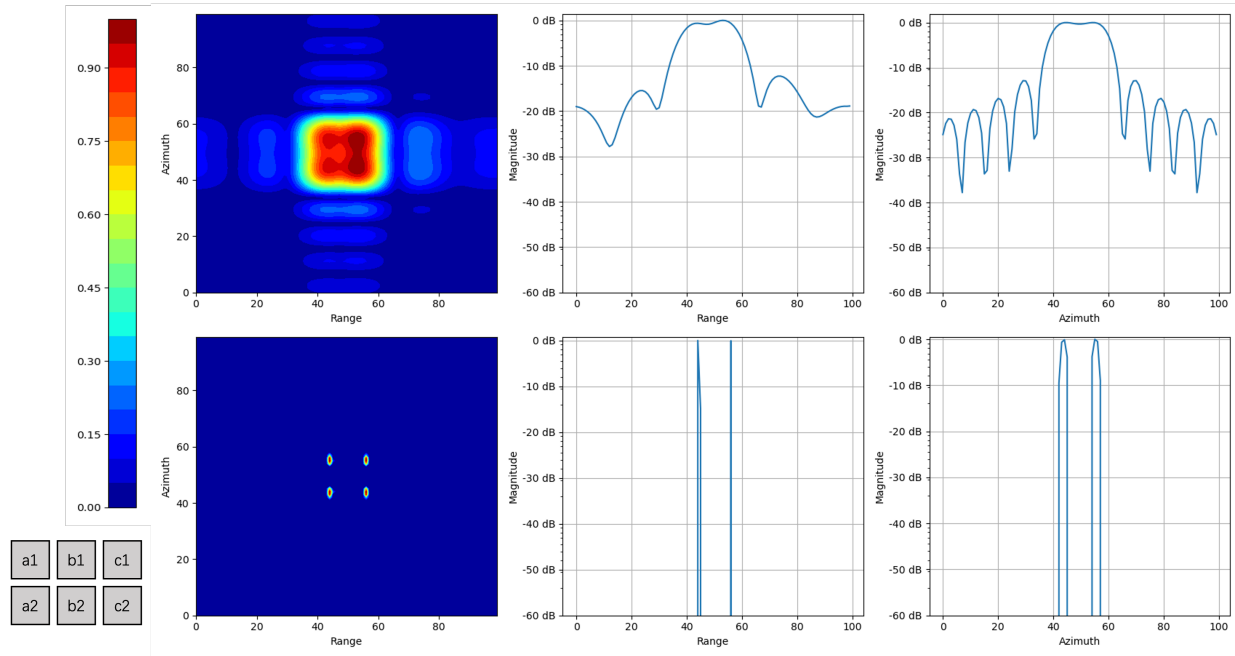
FIGURE 2. Imaging results obtained by different methods for point targets: (a1) BP result,(a2) sPSI results under 100% sampling rates, (b1) and (c1) range profile and azimuth profile of the imaging result by BP, respectively, (b2) and (c2)range profile and azimuth profile of the imaging result by sPSI, respectively.

To explore the performance of the methods in the CS regime, we conducted the performance analysis in terms of the sampling rate (SR), which is defined by the number of observation samples over the number of pixels of the scene. The SR ranges from 25%, 50%, and 100% for all of the CS-based sparse recovery methods (Lasso, PSI, sPSI) and the stopping criterion (relative error of solution) is all set to 10^{-5}. The BP method, however, takes the full data due to its imaging principle. We state that all of the experiments were conducted on the same workstation (Intel Xeon E5-2620 v4, 8 Cores, 2.1GHz, 64GB RAM) only using a single core.

Range	10 km
Height	200 m
Squint angle	0°
Center frequency	5.3 GHz
Bandwidth	70 MHz
Pulse width	0.8 μs
The pulse-repetition frequency	350 Hz
Sampling frequency in range	140 MHz
Field of view of the scene	(100 m, 100 m)
Number of (Range, Azimuth) samples	(300, 300)

TABLE 2. The parameter settings for extended targets simulation.

The imaging results are reported in Figure 3. We can observe that Lasso is worse than BP with more speckle noise present due to the random phase unconsidered, while both PSI and sPSI, sharing comparable super-resolved results, outperform BP. In terms of SR, more details are recovered for both PSI and sPSI
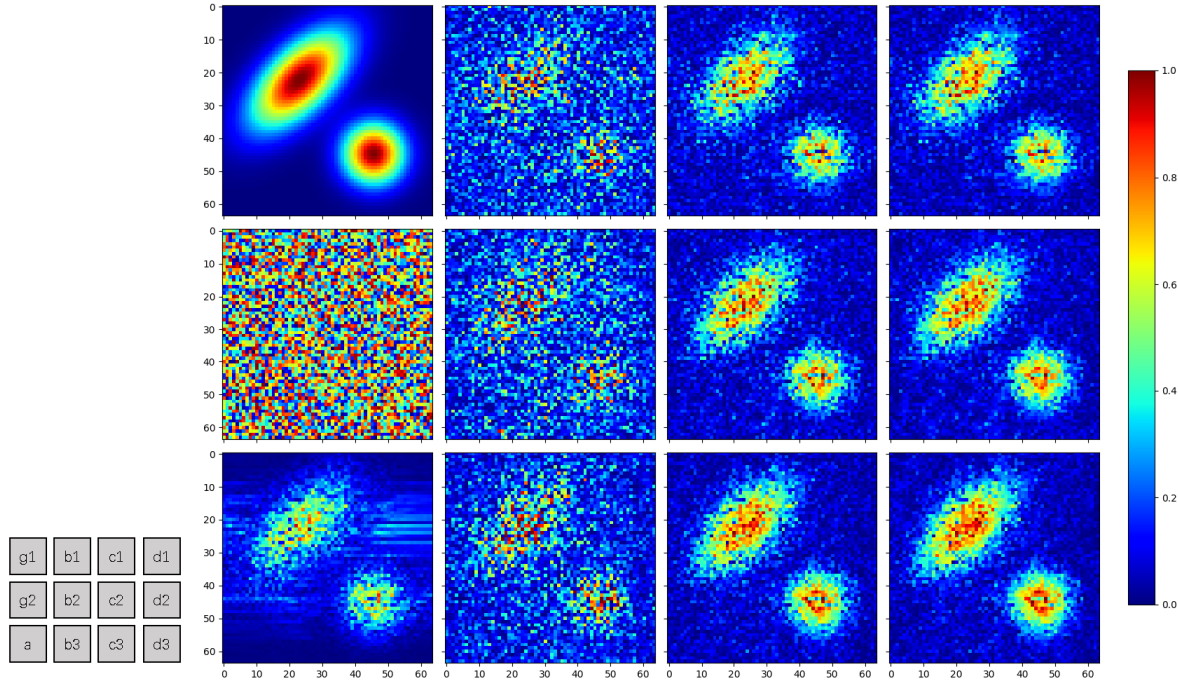
FIGURE 3. Imaging results obtained by different methods with varying sampling rates: (g1) magnitude map of the ground truth, (g2) phase map of the ground truth, (a) BP result (full data), (b1)-(b3) Lasso results under 25%, 50%, and 100% sampling rates from top to bottom, (c1)-(c3) PSI results under 25%, 50%, and 100% sampling rates from top to bottom, (d1)-(d3) sPSI results under 25%, 50%, and 100% sampling rates from top to bottom.

Metrics	SR	BP	Lasso	PSI	sPSI
PSNR (dB)	25%		12.67	17.36	17.97
	50%	16.09	12.41	18.20	19.11
	100%		13.63	19.41	20.30
Time (s)	25%		1523	15440	123
	50%	1360	4718	31461	164
	100%		9145	58649	182

TABLE 3. Quantitative evaluation for different methods. Note that BP uses the full sampling data due to its imaging principle.

from the visual judgment. The detailed quantitative evaluation is reported in Table 3. We can see that the imaging results obtained through PSI are superior to BP by 1.27 dB to 3.32 dB as SR increases, while the Lasso method has limitations regardless of SR. The sPSI method reports similar but slightly better results than PSI as both solve the same optimization problem but sPSI employs the stochastic acceleration for a more efficient execution. As for the execution time, we can clearly see that Lasso and PSI are very computationally expensive which is obvious for optimization-based methods. However, sPSI benefiting from the stochastic acceleration is faster than PSI by at least two orders of magnitude.

5. Conclusions

In this paper, to address an unexplored sphere-constrained sparse SAR imaging problem, we proposed a stochastic sphere-constrained sparse imaging method, dubbed sPSI, to achieve better imaging quality with high efficiency. We conducted two types of numerical simulations to analyze the performance: 1) the point-target simulation showcased the capability of the high resolution of our proposed method compared to the classical methods. 2) the extended target with random phase is simulated to be in line with the practical scenario, and then the results demonstrated that in terms of PSNR sPSI outperforms the classical SAR imaging methods and the state-of-the-art sparse recovery method without phase consideration. Meanwhile, the stochastic average acceleration technique leveraged in sPSI can reduce the high computational cost of iterative-based optimization methods by orders of magnitude. Future work will focus on the study of adaptive hyperparameters tuning strategy and its application in real SAR data.

References

[1] A. Moreira, P. Prats-Iraola, M. Younis, G. Krieger, I. Hajnsek, K.P. Papathanassiou, A tutorial on synthetic aperture radar, IEEE Geoscience and remote sensing magazine, 1 (2013), 6–43.

[2] E.J. Candès, J. Romberg, T. Tao, Robust uncertainty principles: Exact signal reconstruction from highly incomplete frequency information, IEEE Transactions on Information Theory, 52 (2006), 489–509.

[3] D.L. Donoho, Compressed sensing, IEEE Transactions on Information Theory, 52 (2006), 1289–1306.

[4] M. Cetin, W.C. Karl, Feature-enhanced synthetic aperture radar image formation based on nonquadratic regularization, IEEE Transactions on Image Processing, 10 (2001), 623–631.

[5] L. Zhang, M. Xing, C.W. Qiu, J. Li, Z. Bao, Achieving higher resolution isar imaging with limited pulses via compressed sampling, IEEE Geoscience and Remote Sensing Letters, 6 (2009), 567–571.

[6] H. Liu, B. Jiu, H. Liu, Z. Bao, Superresolution isar imaging based on sparse bayesian learning, IEEE Transactions on Geoscience and Remote Sensing, 52 (2013), 5005–5013.

[7] B. Zhang, W. Hong, Y. Wu, Sparse microwave imaging: Principles and applications, Science China Information Sciences, 55 (2012), 1722–1754.

[8] J.H.G. Ender, On compressive sensing applied to radar, Signal Processing, 90 (2010), 1402–1414.

[9] E. Giusti, D. Cataldo, A. Bacci, S. Tomei, M. Martorella, Isar image resolution enhancement: Compressive sensing versus state-of-the-art super-resolution techniques, IEEE Transactions on Aerospace and Electronic Systems, 54 (2018), 1983–1997.

[10] J. Yang, T. Jin, X. Huang, Compressed sensing radar imaging with magnitude sparse representation, IEEE Access, 7 (2019), 29722–29733.

[11] J. Yang, T. Jin, C. Xiao, X. Huang, Compressed sensing radar imaging: Fundamentals, challenges, and advances, Sensors, 19 (2019), 3100.

[12] G. Xu, B. Zhang, H. Yu, J. Chen, M. Xing, W. Hong, Sparse synthetic aperture radar imaging from compressed sensing and machine learning: Theories, applications, and trends, IEEE Geoscience and Remote Sensing Magazine, 10 (2022), 32–69.

[13] J. Fang, Z. Xu, B. Zhang, W. Hong, Y. Wu, Fast compressed sensing sar imaging based on approximated observation, IEEE Journal of Selected Topics in Applied Earth Observations and Remote Sensing, 7 (2013), 352–363.

[14] H. Liu, D. Li, Y. Zhou, T.K. Truong, Joint wideband interference suppression and sar signal recovery based on sparse representations, IEEE Geoscience and Remote Sensing Letters, 14 (2017), 1542–1546.

[15] A. Defazio, F. Bach, S. Lacoste-Julien, Saga: A fast incremental gradient method with support for non-strongly convex composite objectives, Advances in Neural Information Processing Systems, vol. 27, 2014.

[16] D. Driggs, J. Tang, J. Liang, M. Davies, C.B. Schönlieb, Spring: A fast stochastic proximal alternating method for non-smooth non-convex optimization, arXiv preprint arXiv:2002.12266, 2020.

[17] J. Bolte, S. Sabach, M. Teboulle, Proximal alternating linearized minimization for nonconvex and nonsmooth problems, Mathematical Programming, 146 (2014), 459–494.

[18] P.-A. Absil, J. Malick, Projection-like retractions on matrix manifolds, SIAM Journal on Optimization, 22 (2012), 135–158.